PERGAMON

Computers & Fluids 30 (2001) 211–236

computers & fluids

www.elsevier.com/locate/compfluid

A cell boundary element method applied to laminar vortex shedding from circular cylinders

T. Farrant[a,b,1], M. Tan[a,*], W.G. Price[a]

[a]*School of Engineering Sciences, Ship Science, University of Southampton, Highfield, Southampton, SO17 1BJ, UK*
[b]*Computational Engineering and Design Centre, University of Southampton, Highfield, Southampton, SO17 1BJ, UK*

Received 18 February 1999; received in revised form 5 August 1999; accepted 6 March 2000

Abstract

The two-dimensional unsteady incompressible Navier–Stokes equations are solved for flows around arrangements of circular cylinders at Reynolds number 100 and 200. A hybrid boundary element/finite element method is used to discretise the spatial domain together with a second order implicit finite difference approximation in time. The numerical scheme of study is validated for a uniform stream past an isolated circular cylinder by comparing findings with experimental and numerical studies. Both steady state and time dependent solutions were predicted with good agreement. The numerical approach, known here as the cell boundary element method (cell BEM), was also used to solve flows around two cylinders of equal diameter side by side and in tandem. It was found that no modifications to the method were needed to compute the flow field for these connected domains. In-phase and anti-phase vortex shedding modes were found to exist in the flow simulation. These simulations were in excellent agreement with phenomena observed in experiments. Particle simulations, generated from the cell BEM velocity fields, were found to have great similarity with smoke visualisations from experiment. © 2000 Elsevier Science Ltd. All rights reserved.

1. Introduction

The fluid flow around bluff bodies, idealised by a single circular cylinder or by an array of cylinders, has been extensively studied both experimentally and theoretically because of its

* Corresponding author. Tel.: +44-23-8059-2316; fax: +44-23-8059-3299.
E-mail address: mingyi@ship.southampton.ac.uk (M. Tan).
[1] Now at 2H Offshore Ltd., Woking, UK.

0045-7930/01/$ - see front matter © 2000 Elsevier Science Ltd. All rights reserved.
PII: S0045-7930(00)00009-8

relevance to applications in engineering. Examples of investigations are far too numerous to review here but they are associated with flows around flexible risers and tubular offshore structure platforms, flows in heat exchangers, flows around arrays of nuclear fuel rods, chimneys, bridges, etc. To attempt to understand the physical mechanisms arising from the very complex flow behaviour and the interactive loading between an isolated cylinder section and the viscous fluid flow over the Reynolds number (Re) range many experiments have been conducted, see, for example, Sarapkaya and Isaacson [1]. These relate to studies of the relationship between Reynolds number and the frequency of the vortex shedding into the wake as defined by the Strouhal number ($S = fD/U$ where f is shedding frequency, U is the free stream velocity and D is the cylinder diameter). Those readers interested in these fundamental interactive phenomena may consult the detailed review of Williamson [2] who firmly established the existence of a universal Strouhal–Reynolds number relationship from experimental evidence after he, and other authors, accounted for experimental error arising from cylinder vibration, cylinder end effects, shear in the oncoming flow free stream, etc.

Investigations of incompressible flows past multiple cylinders are reported far less in the literature and, because of the increased number of parameters influencing the flow characteristics, they do not exhibit the same systematic approach as adopted in studies of single cylinders. For example, studies involve different arrangements of cylinders (i.e. number, shape, alignment, separation, etc.), different Reynolds number flows, selected boundary conditions, etc. An extensive review of flow interference between two circular cylinders is described by Zdravkovich [3] using the standard classifications of side-by-side, tandem and staggered cylinder arrangements shown in Fig. 1(a)–(c) respectively. In particular, critical spacings separating different flow regimes have been established for the side-by-side and tandem arrangements. The spacing is defined as the minimum gap between the surfaces of the cylinders which is normally nondimensionalised using one cylinder diameter (all the cylinders are of equal diameter). It was observed that for side-by-side cylinders spaced greater than the critical spacing a synchronised shedding regime exists whereas below the critical spacing a deflected flow regime occurs. In the tandem arrangement, if the gap is greater than the critical spacing the upstream cylinder sheds vortices onto the downstream cylinder. Alternatively, if the gap is less than the critical spacing, shedding does not occur from the upstream cylinder.

One of the earliest computational studies of interactive vortex shedding was undertaken by Chang and Song [4]. Two cases, either side of the critical spacing, were considered for the side-by-side arrangement at $Re = 100$. Using a hybrid finite element/finite difference vorticity–stream function formulation they found that it was possible to simulate many of the phenomena associated with this arrangement of equal diameter cylinders. Even a *flipping* between the in-phase and anti-phase shedding modes for the synchronised shedding regime was

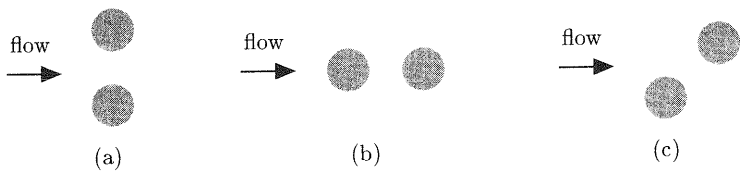

Fig. 1. The (a) side-by-side, (b) tandem and (c) staggered arrangements of two cylinders.

observed in the computation (see, for example, Fig. 2). Furthermore, the numerical scheme produced accurate resolution of the flow features near the cylinders, using the finite element method, together with a computationally inexpensive finite difference procedure for the far-field flow. The use of the finite element method eased the problems of generating a mesh around, and in between, the two cylinders.

Li et al. [5] used the case of two cylinders in tandem at $Re = 100$ as a preliminary study in the development of a Galerkin velocity–pressure finite element formulation. The flow was computed at four different spacings between the cylinder arrangement and comparisons made with experiments, performed at much higher Reynolds numbers, showed similarities with the theoretical findings.

A study of low Reynolds number flow around arrays of cylinders was performed by Johnson et al. [6] using periodic boundary conditions to provide insights into the modelling of heat exchangers and cooling systems. A two-dimensional Petrov–Galerkin vorticity–stream function finite element formulation was used.

A higher Reynolds number investigation ($Re = O(1000)$) was carried out by Mittal et al. [7] for the tandem and staggered arrangements using a Petrov–Galerkin velocity–pressure finite element method. Comparisons of the flow between Reynolds numbers of 100 and 1000 suggested that the critical spacings might be sensitive to Reynolds number and experimental setup with turbulence highly likely in the higher Reynolds number interactive flow. It was concluded that a more comprehensive numerical study was needed to provide understanding of the effects of Reynolds number.

The present paper continues the study of vortex shedding problems from a single cylinder, two cylinders in tandem and also side-by-side. The cell boundary element method, or cell BEM, as developed by Tan et al. [8] is adopted to solve the unsteady fluid problem associated with flow-structure configurations involving groups of dissimilar structures. This utilises unstructured meshes and a primitive-variable formulation. Detailed accounts of the hybrid method, incorporating analytical and numerical components in the overall scheme of study, together with developments of the general approach are described by Tan et al. [8], Price and Tan [9] and Farrant [10]. Hence only a summary of the cell boundary element method is included herein. These previous studies, as described by these investigators, contain a series of validation exercises through detailed comparisons between theoretical predictions derived by the proposed method, findings from other theoretical studies and experimental evidence over a wide range of fluid flow examples. In many ways, this paper continues the validation exercise by focusing on aspects of vortex shedding.

Here results are presented of detailed wake structures behind isolated and two cylinder configurations. In the single cylinder case, the presentation includes a comparison with

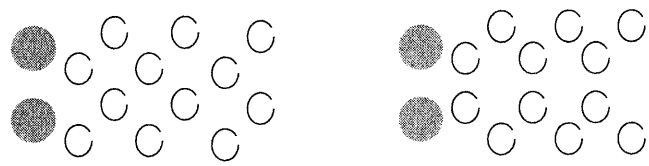

Fig. 2. In-phase (left) and anti-phase (right) shedding modes.

experimental data and the findings of a selection of other computational studies as well as a sensitivity investigation of the effects of boundary conditions and their locations. The flow fields for two circular cylinders of equal diameter in tandem and side-by-side are illustrated, with a more detailed focus on the wake produced in the latter configuration through a comparison of computed simulations and the experimental smoke simulations of Williamson [11]. Both in-phase and anti-phase shedding modes (see Fig. 2) were found to exist naturally in the computation extended over a long time although, with a small perturbation in the flow, they could be induced to pass from one to the other more readily. This feature of the computation was in full agreement with the experimental evidence of Williamson [11]. In addition, the comparison revealed a very satisfactory agreement between the respective wake structures extending approximately 40 cylinder diameters downstream.

2. Mathematical theory

The boundary element method described by Price and Tan [9] treats the nonlinear convective term of the Navier–Stokes equations as a *pseudo body force*. This approach required a solution process involving full matrices and had a negative impact on the overall efficiency and stability of the numerical scheme [12]. To overcome these difficulties, Tosaka and Kakuda [13] developed a generalised boundary element method to tackle nonlinear problems.

This generalised method was used as the basis of an approach by Tan et al. [8] to solve incompressible Navier–Stokes flow problems. In effect, this approach is a hybrid scheme based on the boundary element and finite element methods. That is, instead of introducing the integral equation to the whole fluid-structure system directly, the fluid domain is divided into a large number of cells or elements in a similar discretisation process to the finite element or finite volume methods. The boundary element method is then applied to each cell to generate sets of algebraic equations which consistently represent the Navier–Stokes equations on each cell. Application of continuity conditions, on fluid velocity and surface traction force, at the cell interfaces allows a global system of algebraic equations to be obtained and solved. This global system describes the dynamics of the fluid in the whole domain.

To apply the boundary element method on a cell, the nonlinear term in the Navier–Stokes equations, which models the fluid in each cell, is either linearised locally in each cell for steady state problems or resolved at each time step in time dependent problems. The nonlinear nature of the equation is modelled through iterative processes or time stepping schemes.

The fundamental solution needed for the cell calculation is a modified Oseen solution which has been derived by Price and Tan [9] for two- and three-dimensional problems. The convective velocity involved in the Oseen solution changes not only during the iteration or time stepping but also spatially from cell to cell. This procedure improves numerical stability, speed of numerical convergence since the nonlinear feature of the flow is represented in the fundamental solution.

The cell BEM is a primitive-variable formulation which allows easy application to three-dimensional problems. Furthermore, the use of velocity and surface traction force as the basic unknowns provides a convenient way of expressing boundary conditions.

In this paper the formulation is described briefly with particular emphasis on its use in two-

dimensional, time dependent problems. For a complete description of the method for steady state and time dependent problems with validation examples see Tan et al. [8].

2.1. Governing equations and integral equation

The fluid domain is represented by an unstructured cell idealisation with individual cell domain Ω and surface Σ as illustrated in Fig. 3. If the fluid is assumed incompressible, the Navier–Stokes equation and continuity equation describing the fluid flow velocity, $v'(x', t')$, and pressure, $p'(x', t')$, are given respectively by

$$\frac{\partial v'_j}{\partial t'} + \left(v'_j v'_k\right)_{,k'} + \frac{1}{\rho'} p'_j - \frac{1}{\rho'}\left[\mu'\left(v'_{j,k'} + v'_{k,j'}\right)\right]_{,k'} = 0, \tag{1}$$

$$v'_{j,j'} = 0 \tag{2}$$

Here density and viscosity are denoted by ρ' and μ', respectively, the prime ($'$) indicates a dimensional quantity and a tensor index notation with summation convention is used to keep mathematical expressions compact. An example of the notation is given by the convective term, taken from Eq. (1),

$$\left(v'_j v'_k\right)_{,k'} = \sum_{k=1} \frac{\partial\left(v'_j v'_k\right)}{\partial x'_k}.$$

The upper limit of the summation in the expression takes the value of 2 or 3 for two- and three-dimensional problems, respectively.

In order to non-dimensionalise Eqs. (1) and (2), a change of variable is made using the definitions

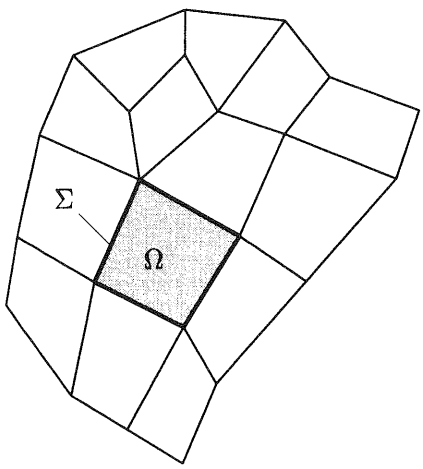

Fig. 3. A cell within the global fluid domain idealised in an unstructured manner.

$$x_j = \frac{x_j'}{L'}, \quad t = \frac{U'}{L'}t', \quad v_j = \frac{v_j'}{U'}, \quad p = \frac{p'}{\rho' U'^2}.$$

Here L' and U' are the characteristic length and velocity, respectively. For bluff body flows in a uniform stream, normally the characteristic length is taken as the largest body dimension across the stream and the characteristic velocity is that of the stream. Eqs. (1) and (2) now become

$$\dot{v}_j + (v_j v_k)_{,k} + p_{,j} - \left[\nu_e (v_{j,k} + v_{k,j})\right]_{,k} = 0, \tag{3}$$

$$v_{j,j} = 0, \tag{4}$$

where $\nu_e = 1/Re$ and Reynolds number $Re = (\rho' U' L')/\mu'$.

Before formation of an integral equation involving the Navier–Stokes equations, it is beneficial both analytically and for enhanced computational efficiency to introduce a scheme to resolve the nonlinear convective term in Eq. (3). For time dependent problems this can be achieved using a time marching process. Two possible time marching procedures are as follows,

- *First order scheme.* To maintain an accuracy of order Δt in the $(n+1)$th time step, the time marching scheme takes the form,

$$h_j + \left(v_j \tilde{v}_k\right)_{,k} + p_{,j} - \left[\nu_e (v_{j,k} + v_{k,j})\right]_{,k} = 0 \tag{5}$$

  where $h_j = \frac{1}{\Delta t}[v_j - v_j^{(n)}]$ and $\tilde{v}_k = v_k^{(n)}$ is the velocity from the nth time step.
- *Second order scheme.* To maintain an accuracy of second order, Δt^2, in the $(n+1)$th time step, the time marching scheme is similar to the first order scheme except that a contribution from the velocity field at the $(n-1)$th time step is also included. In this case, the time stepping scheme takes the form,

$$h_j = \frac{1}{2\Delta t}\left[3v_j - 4v_j^{(n)} + v_j^{(n-1)}\right]$$

and

$$\tilde{v}_k = 2v_k^{(n)} - v_k^{(n-1)}.$$

Regardless of the time marching scheme employed it is possible to form an integral equation using the modified form of the Navier–Stokes equations (Eq. (5)). Integrating over the cell domain Ω, while incorporating two arbitrary weighting functions v_{sj}^* and p_s^*, and applying Gauss's theorem leads to the following integral equation [12].

$$\int_\Omega \left\{ v^*_{sj}\left[h_j + \left(v_j\tilde{v}_k\right)_{,k} + p_{,j} - \left(\nu_e\left(v_{j,\,k} + v_{k,\,j}\right)\right)_{,k}\right] + p^*_s v_{j,\,j} \right\} \mathrm{d}\Omega + \int_\Omega \left\{ v_j\left[\tilde{v}_k v^*_{sj,\,k} + p^*_{s,\,j} + \left(\nu_e\left(v^*_{sj,\,k} + v^*_{sk,\,j}\right)\right)_{,k}\right] + p v^*_{sj,\,j} \right\} \mathrm{d}\Omega$$

$$= \int_\Sigma \left[v_j\left(\tilde{v}_k n_k v^*_{sj} + R^*_{sj}\right) - R_j v^*_{sj}\right] \mathrm{d}\Sigma + \int_\Omega h_j v^*_{sj}\,\mathrm{d}\Omega. \tag{6}$$

In this integral equation, n is the outward normal to the surface Σ. Furthermore, $R_j = -pn_j + \nu_e(v_{j,\,k} + v_{k,\,j})n_k$ represents the jth component of the dimensionless traction force on the boundary surface. The variable R^*_{sj} is defined as

$$R^*_{sj} = p^*_s n_j + \nu_e\left(v^*_{sj,\,k} + v^*_{sk,\,j}\right)n_k.$$

The integral equality in Eq. (6) is valid for any functions v_j, p, v^*_{sj} and p^*_s provided that all terms involved are integrable. Since the weighing functions v^*_{sj} and p^*_s are arbitrary it is possible to choose them in such a way as to satisfy the equations:

$$\tilde{v}_k v^*_{sj,\,k} + p^*_{s,\,j} + \left(\nu_e\left(v^*_{sj,\,k} + v^*_{sk,\,j}\right)\right)_{,k} = -\delta_{sj}\Delta\left(x_j - \xi_j\right), \tag{7}$$

$$v^*_{sj,\,j} = 0, \tag{8}$$

where δ and Δ are Kronecker and Dirac delta functions, respectively. The solution of Eqs. (7) and (8) is referred to as the fundamental solution and represents the response of the system to a point excitation. Choosing the functions to satisfy Eqs. (7) and (8), according to the boundary element method, considerably simplifies Eq. (6) to

$$C(\xi)v_s(\xi, t) + \int_\Sigma v_j\left(\tilde{v}n v^*_{sj} + R^*_{sj}\right)\mathrm{d}\Sigma = \int_\Sigma R_j v^*_{sj}\,\mathrm{d}\Sigma - \int_\Omega h_j v^*_{sj}\,\mathrm{d}\Omega \tag{9}$$

where

$$C(\xi) = \begin{cases} 0 & \text{if } \xi \notin (\Omega \cup \Sigma), \\ \dfrac{1}{2} & \text{if } \xi \in \Sigma, \\ 1 & \text{if } \xi \in \Omega \end{cases} . \tag{10}$$

In Eq. (9) the velocity anywhere in the cell is expressed as surface integrals of velocity v and traction R on the cell boundary as well as a domain integral which can also be calculated from the values of velocity on the boundary. Therefore, Eq. (9) represents a relationship between the cell velocity field and the surface traction force.

A description of the derivation process for the fundamental solution is given by Tan et al. [8] and further details are discussed by Price and Tan [14]. This description will not be repeated here. However, it should be noted that, to simplify the process of solution of Eqs. (7) and (8), a further approximation is introduced to replace the unknown convective velocity $\tilde{v}_k$ by a cell

average velocity u_k. This was shown to have an insignificant effect on overall solutions [8] after undertaking an extensive number of numerical tests.

2.2. Numerical modelling and the cell equations

To solve a fluid-flow problem the domain is discretised into a large number of cells in the unstructured form as shown in Fig. 3. For each cell, it is possible to approximate the integral equation (9) through adoption of assumed distributions of the unknowns v and R based on their values at collocation points on the cell boundary. This procedure is developed from the standard boundary element discretisation methods, see, for example, Brebbia [15] and Brebbia and Walker [16,17]. The introduction of this approximation procedure allows a set of algebraic equations to be obtained from the the integral equation (9). To illustrate this process by way of example, a discussion follows for the two-dimensional, time dependent case where the first-order time stepping scheme is used and cells are restricted to quadrilateral shapes with collocation points at the centre of each edge.

A typical cell is shown in Fig. 4. The collocation points and edges are assigned a common local numbering system as there is only one control point per edge. Also shown is a local coordinate system η_1 and η_2 which is used for the interpolation functions. Applying this cell structure to the integral equation (9) results in the following approximate form

$$C(\xi)v_s(\xi,t)+\sum_{l=1}^{l=4}\int_l\left(unv_{sj}^*+R_{sj}^*\right)\sum_{i=1}^{i=4}N_v^{(i)}v_j^{(i)}\,\mathrm{d}\Sigma-\frac{1}{\Delta t}\int_\Omega\sum_{i=1}^{i=4}N_v^{(i)}v_j^{(i)}v_{sj}^*\,\mathrm{d}\Omega$$

$$=\sum_{l=1}^{l=4}\int_{(l)}v_{sj}^*\sum_{i=1}^{i=4}N_r^{(i)}R_j^{(i)}\,\mathrm{d}\Sigma+\frac{1}{\Delta t}\int_\Omega\sum_{i=1}^{i=4}N_a^{(i)}v_j^{(n)}v_{sj}^*\,\mathrm{d}\Omega. \tag{11}$$

Here, $N_v^{(i)}$, $N_r^{(i)}$ and $N_a^{(i)}$ are sets of interpolation polynomials for the velocity field v_j, the surface traction force R_j and the velocity from the previous time step $v_j^{(n)}$ respectively. The subscript a is used because the integral arises due to the presence of the acceleration term in the Navier–Stokes equations. The index $l=1,2,3,4$ and indicates a line integration along each edge of the cell. However, the index i, also varies from one to four but moves through the

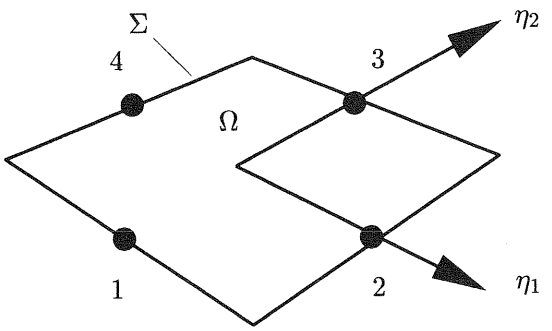

Fig. 4. The two-dimensional quadrilateral cell definition.

collocation points and the corresponding interpolation functions as required by the integration. For the velocity field, the interpolation functions are chosen as follows.

$$N_v^{(1)} = \frac{1}{4}\left[(1-\eta_2)^2 - \eta_1^2\right], \quad N_v^{(2)} = \frac{1}{4}\left[(1+\eta_1)^2 - \eta_2^2\right],$$

$$N_v^{(3)} = \frac{1}{4}\left[(1+\eta_2)^2 - \eta_1^2\right], \quad N_v^{(4)} = \frac{1}{4}\left[(1-\eta_1)^2 - \eta_2^2\right].$$

Other more specialised interpolation functions are employed for the surface traction force R_j and the velocity from the previous time step $v_j^{(n)}$. These functions were chosen according to considerations of accuracy and ease of evaluation of the respective integrals. For a more detailed description of this and the integration of the fundamental solution see Tan et al. [8]

When ξ in Eq. (11) moves to the coordinates of each collocation point in turn and the index s allowed to take the values 1 and 2 (because of two-dimensions), eight simultaneous algebraic equations are generated for the cell. Therefore, if the superscript e denotes the eth cell, the eight algebraic equations can be expressed in the form

$$A_v^{(e)} V^{(e)} = A_r^{(e)} R^{(e)} + b^{(e)}.$$

Here, $V^{(e)}$ and $R^{(e)}$ are column arrays of the velocity field and surface traction force components at the collocation points. The 8×8 matrix $A_v^{(e)}$ groups coefficients which arise due to the evaluation of the two integrals on the left-hand side of Eq. (11) involving the velocity at the collocation points. The 8×8 matrix $A_r^{(e)}$ includes coefficients from the boundary integral on the right-hand side of Eq. (11) containing the values of the surface traction force at the collocation points. The single column array $b^{(e)}$ contains entries evaluated from the domain integral incorporating the contribution of the velocity from the last time step, $v_j^{(n)}$.

In order to construct a global system of equations to solve for the velocity field, using the eight-cell equations, an expression for $R^{(e)}$ is obtained in the form

$$R^{(e)} = C^{(e)} V^{(e)} - d^{(e)}, \tag{12}$$

where $C^{(e)}$ and $d^{(e)}$ are solutions of the equations

$$A_r^{(e)} C^{(e)} = A_v^{(e)}, \qquad A_r^{(e)} d^{(e)} = b^{(e)}. \tag{13}$$

Because the flow is incompressible, the matrix $A_r^{(e)}$ is nearly singular. Therefore, the singular value decomposition method is used to obtain $C^{(e)}$ and $d^{(e)}$ [18]. Algebraic cell equations (as defined by Eq. (12)) can be obtained for every cell in the mesh. The combination of the equation sets from all the cells allow solution of the global fluid problem.

2.3. The global equations

To solve the global fluid problem the cell equations are assembled into a global system using cell interface conditions applied at the collocation points. For the surface traction force R, the forces must be equal and opposite to one another on common collocation points between

neighbouring cells. Additionally, the velocity v must be equal at common collocation points. Mathematically this can be expressed as

$$R^{(i)} + R'^{(i')} = 0 \quad \text{and} \quad v^{(i)} = v'^{(i')}, \tag{14}$$

where $R^{(i)}$, $R'^{(i')}$, $v^{(i)}$ and $v'^{(i')}$ are the values of the traction and velocity on the same collocation point belonging to different cells.

The global system of equations is assembled according to a global order which is defined using a consecutive numbering system for the collocation points in the mesh. This numbering process is identical to that used in the construction of the stiffness matrix in a finite element analysis of structures (see, for example, Cook et al. [19]). Using the inter-cell conditions, the global numbering system and the cell equation sets generated by Eq. (12), a global system of algebraic equations describing the velocities at the collocation points is created. That is,

$$DV = F, \tag{15}$$

where V is the array of velocity values on the collocation points in the global order, D is constructed from the coefficients in $C^{(e)}$ (see Eq. (12)) and F represents the contributions from $b^{(e)}$.

Before solution of the fluid problem it is necessary to specify boundary conditions on the global domain. For this formulation, there are two kinds of boundary conditions which can be applied conveniently. Namely, either the velocity v or the traction force R may be specified.

Specification of the velocity, for example as a no-slip condition on a body surface, results in the calculation of the traction force for that collocation point. To do this, Eq. (15) is modified by substituting the known value of v and moving all the column of values generated from the product of the velocity and its corresponding matrix coefficients to the right-hand side. These values are accumulated in the appropriate row of F. The diagonal element of the matrix D, corresponding to the specified boundary condition, is then set to the value of 1 in order that the unknown traction force value is calculated in place of the velocity.

When a traction force boundary condition is specified, its effect is directly evaluated by substituting its value in the right-hand side. Specification of the traction force on the fluid boundary problem is appropriate, for example, at out-flow boundaries where the details of the velocity at that point are not known.

Each cell only interacts directly with its neighbours through shared collocation points. This feature of the scheme leads to the global equation system matrix D being symmetrical in form although the values of its nonzero entries are not. For such matrices, the skyline methods of matrix storage is efficient [20].

3. Numerical experiments with circular cylinders

An extensive validation of the cell boundary element method for steady state problems was undertaken by the authors using comparisons with analytical and experimental benchmarks such as Couette flow, internal flows and the flow over a backward facing step [8]. Here results are presented extending the validation process and the method to solve laminar vortex

shedding flows around bluff bodies in isolation and in close proximity to one another. The steady state solutions discussed herein are an outcome of the time dependent algorithm and not derived from an assumed steady state solution expression.

3.1. Isolated circular cylinder

The flow around an isolated circular cylinder has been much studied and it remains an active area of research. Williamson [2] presents a review of recent theoretical and experimental investigations. The flow in the Reynolds number range $Re \leq 260$ is of particular interest for the validation of numerical schemes solving the Navier–Stokes equations because the vortex shedding flow remains laminar and well ordered. In the case of two-dimensional flow computations, two different types of solution exist because the flow bifurcates at $Re \approx 49$. The first solution relates to a steady state symmetric flow and this has been calculated by Fornberg [21] for selected Reynolds numbers. In this numerical computation based on a purposely created finite-difference numerical scheme of study, symmetry properties were assumed in the mathematical model requiring the use of a half cylinder only and the developed refined mesh of the surrounding fluid utilised the geometric characteristics of the circular cylinder and was specific to this problem. This steady state symmetric solution is less stable than the asymmetric, time dependent flow solution which describes a vortex street wake. For this vortex shedding solution, the relation between the Strouhal shedding frequency S as a function of Reynolds number has been determined to a level of 1% error by Williamson [2].

Using the time dependent cell BEM at $Re = 100$ with no preconceived assumption on symmetry, the whole cylinder was used and the surrounding fluid meshed with no particular reference to the circular cylinder which, in reality, could have been of arbitrary shape as demonstrated by Tan et al. [8] and Farrant et al. [22]. For this isolated circular cylinder–fluid flow interaction, it was found that both solutions were present with the *steady state* solution persisting for some time until the vortex shedding established itself and a vortex street resulted. Reproduction of the results of Fornberg [21] and those for the experimental Strouhal frequency were used as validation of the cell BEM at a Reynolds number of $Re = 100$.

3.1.1. Isolated cylinder at Reynolds number of 100

At this Reynolds number, numerical evidence confirms the existence of both steady and unsteady flow solutions. Fig. 5 illustrates these two solutions and the sequence of events occurring in passing from one to the other. Initially, a fully developed steady state solution symmetric about the longitudinal plane was formed. The characteristics of either vortex generated were found to correlate closely with the findings of Fornberg in shape, length, breadth, etc. This symmetric, steady state solution persisted for some time until the vortex shedding established itself and a vortex street wake was created. During this transition it was observed that a small disturbance occurred far downstream in the symmetric wake and as the computation continued in time the free shear layers became distorted and folded at the tail of the separation bubble. As time passed, the edge of the separation bubble at the tail became repeatedly folded with oscillations in the wake becoming more vigorous. Eventually the folds in the edge of the bubble rolled up and were carried downstream. This represented the start of

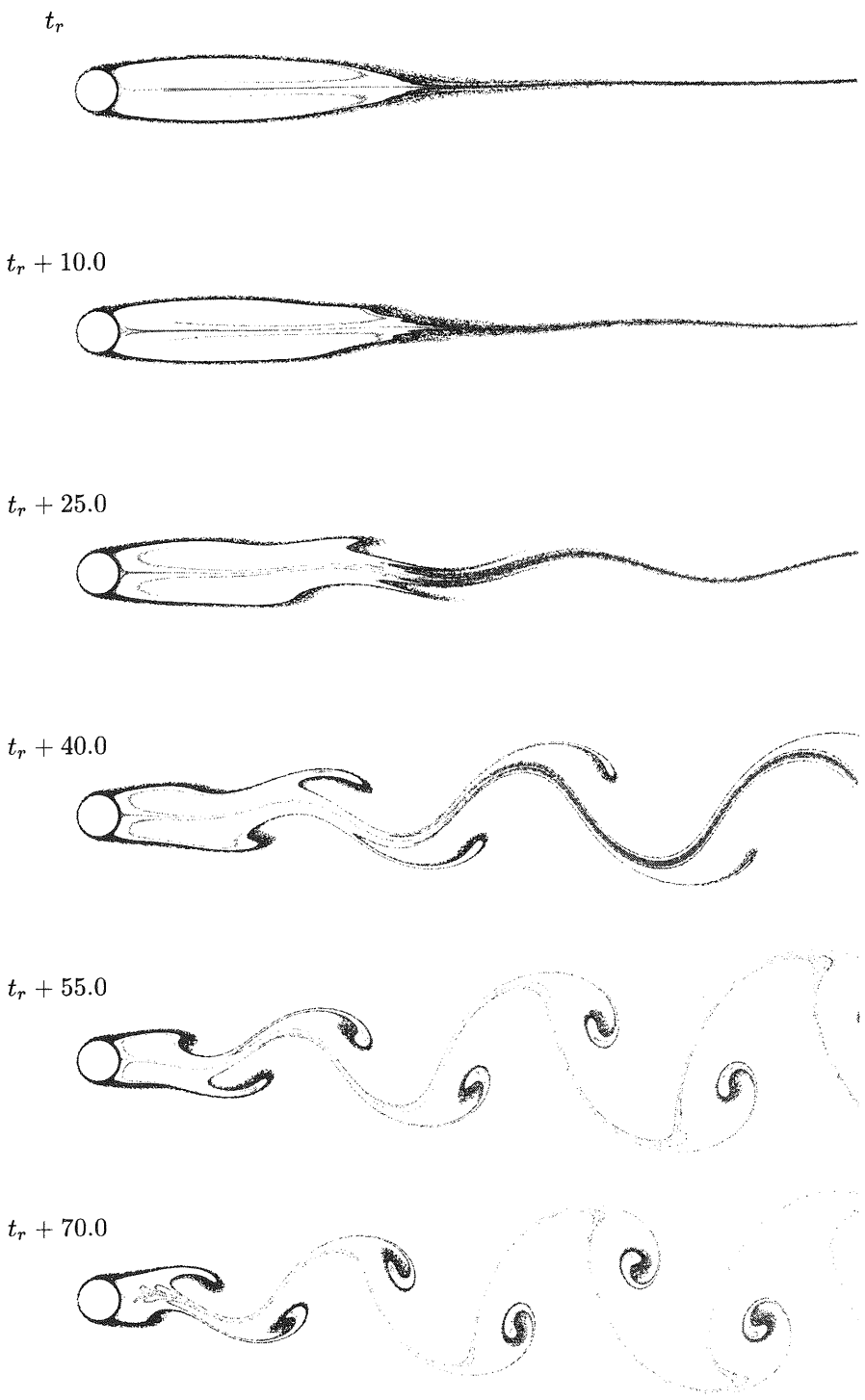

Fig. 5. The transition of the symmetric steady state solution into the more stable vortex shedding solution for the flow around an isolated circular cylinder at Reynolds number $Re = 100$. The time t_r is an arbitrary non-dimensional reference time just before the onset of shedding.

the vortex shedding. As time progressed the shed vortices became stronger until a full vortex street was established.

A typical time history of the calculated lift coefficient C_D affecting the isolated cylinder of diameter D is shown in Fig. 6. To achieve this result from the proposed numerical scheme of study, Fig. 7 illustrates the chosen computational domain, the boundary conditions adopted and the parameters x_f, x_b and x_s which denote the positions of the domain boundaries at the front, back and sides, respectively, relative to the cylinder. During this numerical experiment at $Re = 100$, the symmetric wake solution existed for sufficient time to allow a comparison with the specific steady state results derived by Fornberg [21].

To determine the effect of the domain boundaries on the solution, a mesh of intermediate refinement was chosen and the extents of the mesh systematically varied one at a time. In each case, the *steady state* drag coefficient was calculated by accelerating the flow to the required strength and then time stepping. If time stepping was continued too far the cylinder would start shedding vortices. However, at $Re = 100$ it was found that a reliable estimate of the *steady state* drag coefficient could be determined. This systematic study revealed that the rate of change of the drag coefficient (such as $\partial C_D/\partial x_b$) reduced exponentially with domain extent parameters x_f, x_b and x_s. This variation is illustrated in Fig. 8 where the data form straight lines on a log-linear scale. Using this exponential behaviour it was possible to fit a model equation to the data. For example, in the case of the back boundary x_b,

$$\frac{\partial C_D}{\partial x_b} = -a \exp(-bx_b), \tag{16}$$

where a and b are coefficients determined from the curve fit. Integration of Eq. (16) provides an estimate of the error due to the boundary. For example,

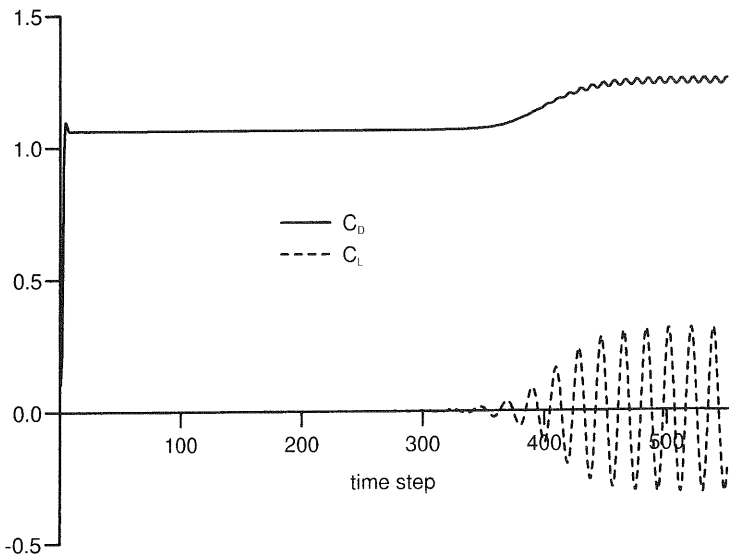

Fig. 6. A typical force coefficient time history for an isolated cylinder at $Re = 100$. The figure shows acceleration of the flow to a uniform stream, development of the symmetric wake and the onset of asymmetry through bifurcation.

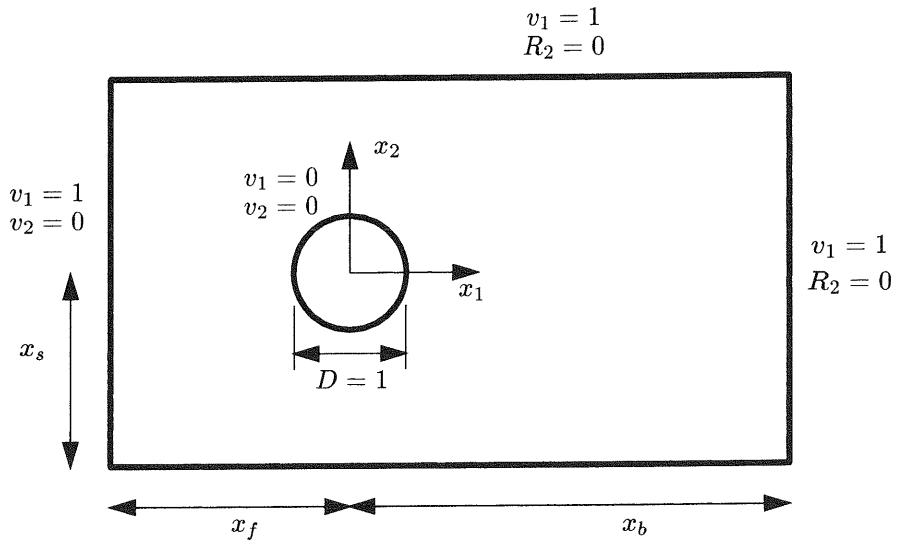

Fig. 7. Computational domain and boundary condition definition.

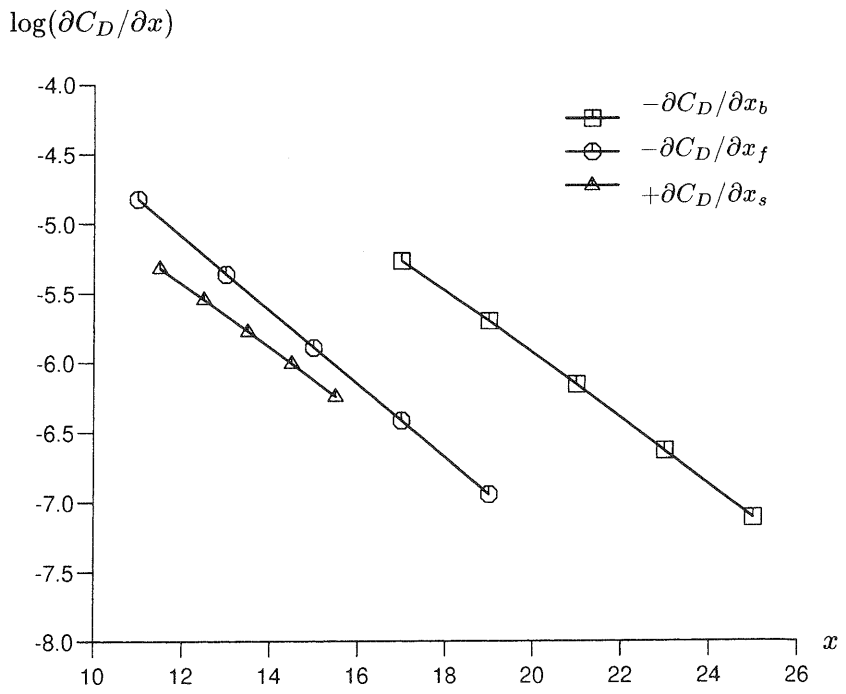

Fig. 8. The rate of change of the steady state drag coefficient with boundary location, $\partial C_D/\partial x$. The location of the front, back and side boundaries of the mesh are denoted by x_f, x_b and x_s, respectively.

$$\varepsilon(x_d) \equiv \frac{|C_D(\infty) - C_D(x_b)|}{|C_D(\infty)|} \approx \frac{a}{bC_D(x_b)}\exp(-bx_b),$$

where ε is the error and $C_D(\infty)$ is the drag coefficient value if the domain boundary is taken to infinity.

From such considerations values of x_f, x_b and x_s were chosen to be 20, 17 and 13, respectively, corresponding to an individual error for each boundary of approximately 1%. These values satisfy criteria proposed by Behr et al. [23] and Tezduyar and Shih [24] in their numerical experiments to evaluate the dependence and influence of the location of boundaries on flow characteristcs. Their studies and the present investigation provide independent corroborative evidence on numerical accuracy of calculation and overall conclusion. Furthermore, using this choice of x_f, x_b and x_s values it was found that significant error cancellation occurred. This was because the value of C_D was under predicted by the effect of x_s and over predicted by the effects of x_f and x_b.

After examining the sensitivity of the domain boundaries on the solution, two other boundary condition combinations were considered. The three combinations are listed in Table 1. The boundary conditions in case (i) were the least restrictive, setting the surface traction force R_j to zero over all of the boundary except at the inlet. Case (iii) was the most restrictive with the velocity set to the uniform stream value all around the boundary. The case (ii) boundary conditions represented an intermediate combination as a compromise for modelling an infinite domain. It was found that the more restrictive boundary conditions generally resulted in a higher drag coefficient and the changes in this value were of a few percent. The intermediate boundary conditions of case (ii) were chosen for subsequent computations.

Mesh independence was verified by varying the number of collocation points and assessing the affect on the drag coefficient. These data are shown in Table 2 and compared with the value calculated by Fornberg [21]. The agreement of these two solutions derived differently was extremely close thus providing a further measure of validation of the cell boundary element method. The mesh, consisting of 21,600 collocation points, was the one used in the previous studies of boundary conditions and their locations.

Having performed a sensitivity study of the mesh and boundary conditions using the steady state solution of Fornberg [21] as a benchmark, a computation using the mesh with 21,600 collocation points was continued until vortex shedding was established. The influence of time step size Δt was examined by successively reducing its value and then allowing shedding to settle down to a periodic state again. The changes in the force coefficients C_D and C_L and the Strouhal shedding frequency S due to time step size are summarised in Table 3. The Strouhal

Table 1
The effect of different boundary conditions on the steady state drag coefficient C_D at $Re = 100$

Case	Front	Sides	Back	C_D
i	$v_1 = 1$, $v_2 = 0$	$R_1 = 0$, $R_2 = 0$	$R_1 = 0$, $R_2 = 0$	1.05
ii	$v_1 = 1$, $v_2 = 0$	$v_1 = 1$, $R_2 = 0$	$v_1 = 1$, $R_2 = 0$	1.06
iii	$v_1 = 1$, $v_2 = 0$	$v_1 = 1$, $v_2 = 0$	$v_1 = 1$, $v_2 = 0$	1.08

Table 2
A comparison of the steady state drag coefficient at $Re = 100$ for five meshes of increasing refinement

Method	Number of collocation points	Drag coefficient C_D
Cell BEM	8244	1.11
	17,336	1.06
	21,600	1.06
	26,512	1.06
	Number of grid points	
Fornberg [21] (half cylinder)	26,353	1.060

frequency determined by Williamson [25], to a 1% level of accuracy, is also shown in the table and with good agreement.

3.1.2. Isolated cylinder at Reynolds number of 200

At this Reynolds number the *steady state* symmetric wake solution is not sufficiently stable to establish itself within the time stepping numerical scheme of study, before the vortex shedding starts. It is thus not possible to determine the effect of the boundaries by evaluation of the *steady state* drag as at $Re = 100$ and, therefore, a sensitivity analysis of the shedding solution to the boundary location was investigated. This was achieved by performing many computations, progressively moving the location of one boundary at a time. Each was run until periodic shedding was established. The data generated from these tests are shown in Fig. 9. From this study, it was found that the lift force was most sensitive to the extent of the mesh while the shedding frequency was quite robust. Furthermore, perhaps because of the periodic wake, the upstream boundary had slightly more effect than the one downstream. In the light of this, the dimensions of the mesh were chosen to be $16D$ front, $14D$ back and $10D$ at the sides. This choice provided a good compromise between computational cost and accuracy confirming the findings of Behr et al. [23] and Tezduyar Shih [24].

To check the effect of boundary conditions, three sets were applied, of different restrictiveness, in the same way as described in the previous section. These results are shown in Table 4. The trend is similar to the one observed in the steady state case. That is, the more restrictive boundary conditions corresponded to increased values of C_D, C_L and S. The choice

Table 3
The convergence of the second order time stepping scheme for the key vortex shedding parameters of the forces acting on an isolated cylinder at $Re = 100$

Δt	S	Error (%)[a]	C_D (time average)	C_L (peak to peak)
0.4	0.169	3.0	1.45	1.01
0.2	0.166	1.2	1.35	0.73
0.1	0.164	0.0	1.33	0.67
0.05	0.163	0.6	1.33	0.66
0.025	0.163	0.6	1.33	0.66

[a] Strouhal shedding frequency, S is 0.164 [22].

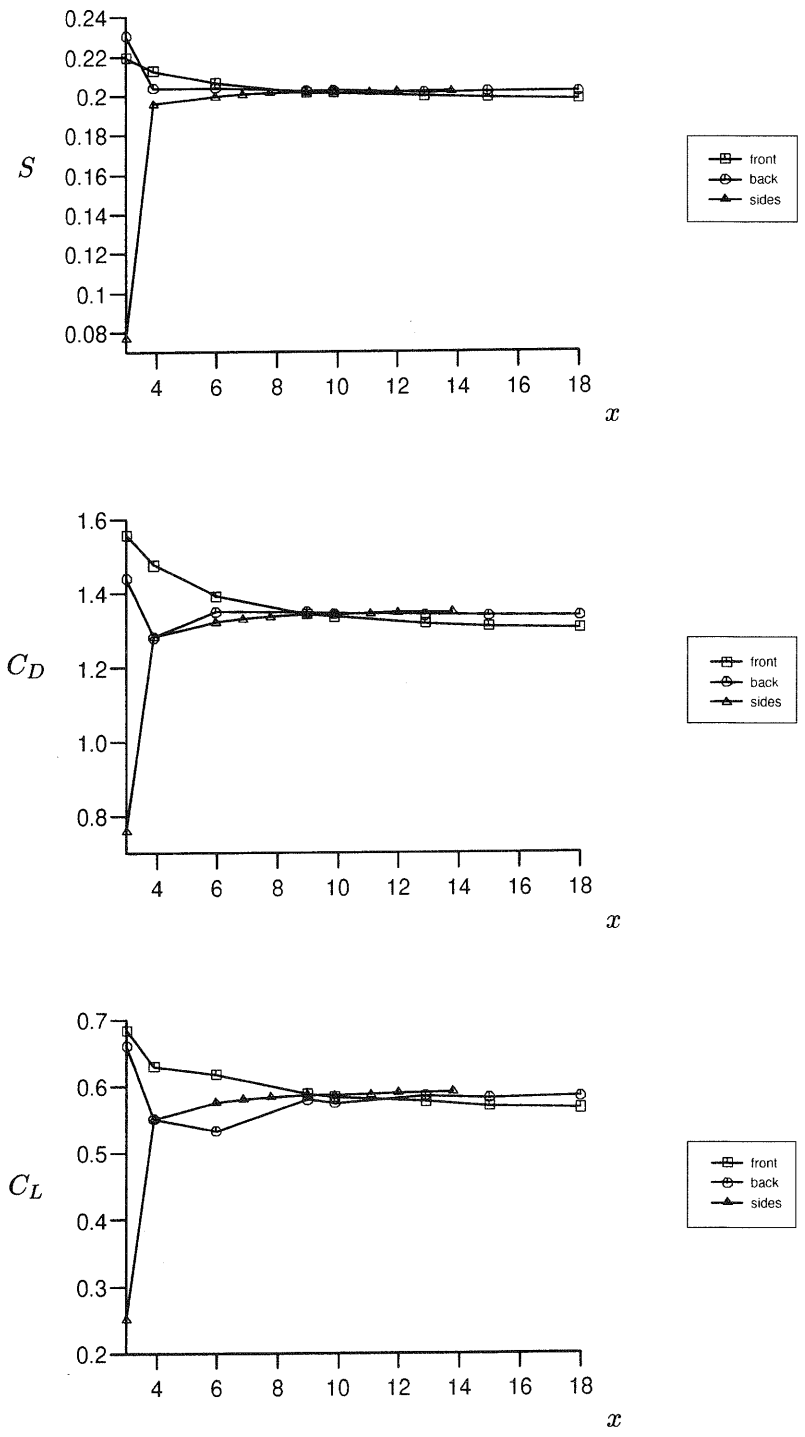

Fig. 9. The effect of the front, back and side boundary locations on the Strouhal shedding frequency S, drag coefficient C_D and lift coefficient C_L for a circular cylinder at $Re = 200$.

Table 4
The effect of different boundary conditions on the vortex shedding at $Re = 200$[a]

Case	S	C_D (time average)	C_L (peak to peak)
i	0.195	1.34	1.39
ii	0.196	1.36	1.42
iii	0.200	1.39	1.43

[a] See Table 1 for definition of boundary condition cases.

of boundary conditions were found to affect C_D, C_L and S by approximately 2% from an average parameter value.

Mesh refinement checks were performed using five meshes. The effect on vortex shedding is shown Table 5. From these data it was decided to use the third mesh (8033 collocation points) for further computations as this provided a compromise between accuracy and computational cost. As with the $Re = 100$ case, the time step size was altered over a range of values and the results are shown in Table 6. It was found that, as long as the time step was at least as small as 0.1, the solution changed less than a few percent for all values in Table 6.

When the time averaged drag value was calculated by integrating over the time period, the positive and negative deviations from the mean did not always have the same magnitude. That is, the time average was not the same as the mean of the peak values. This difference was found to disappear with decreasing time step, which is shown in Fig. 10. The poor resolution of the oscillation in drag is probably due to the frequency being twice that of the lift. In spite of this, a time step of $\Delta t = 0.1$ was chosen for all further computations because of computational costs. In all subsequent computations it must be remembered that this slight error exists which, as a percentage of the time average value, is the order of 1%. It was found that for the lower Reynolds number case, $Re = 100$, the effect of this error was too small to be detected.

Comparable experimental data for shedding frequency at $Re = 200$ for a two-dimensional flow are not available. This is because, in experiment, it is found that around $Re = 180$ a three-dimensional instability occurs which results in a discontinuity in the variation of Strouhal number versus Reynolds number relationship [25]. In spite of this, numerous computations

Table 5
The effect of mesh refinement on the shedding frequency S, drag coefficient C_D and lift coefficient C_L for an isolated cylinder at $Re = 200$[a]

Number of collocation points	S	C_D (time average)	C_L (peak to peak)
2907	0.193	1.47	1.51
6037	0.193	1.39	1.50
8033	0.196	1.36	1.42
11358	0.196	1.36	1.42
15295	0.196	1.37	1.45

[a] The second order time stepping scheme was used.

Table 6
The convergence in time, for the second order time stepping scheme, of key vortex shedding parameters for an isolated cylinder at $Re = 200$

Δt	S	C_D (time average)	C_L (peak to peak)
0.2	0.203	1.39	1.46
0.1	0.196	1.36	1.42
0.05	0.196	1.36	1.40
0.025	0.196	1.36	1.43

have been carried out by different authors, and a selection of results are shown in Table 7. These computations show fair agreement with those of the cell BEM, with the exception of Li et al. [5]. Furthermore, it was found that for the cell method the steady state symmetric wake solution at this higher Reynolds number did not establish itself for long enough in time to allow a meaningful comparison with the findings of Fornberg [21].

3.2. Two circular cylinders

Comparison of the cell BEM for flows around two circular cylinders is less straight forward. Although comprehensive and useful reviews of experimental work have been produced [3] there

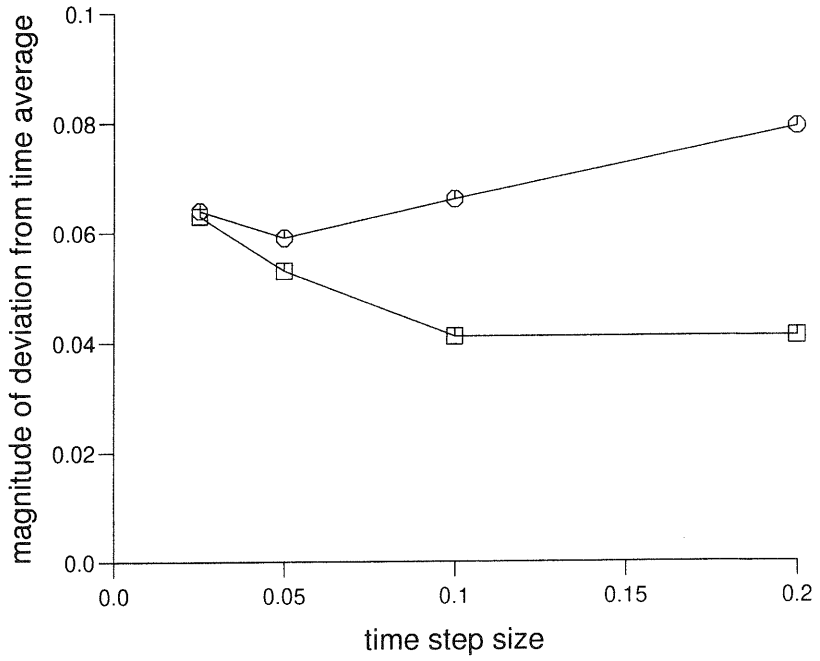

Fig. 10. An illustration of the influence of the time step size to the variation in the calculated magnitudes of the positive and negative deviations from their time averaged value. The square markers indicate the variation of the maximum positive deviation and the circles that of the maximum negative deviation.

is only limited information which is suitable for validation in the laminar regime. Perhaps the most useful data are the wind tunnel smoke visualisations of Williamson [11] for two circular cylinders side-by-side. It should be noted that the flow visualisations from the water channel provided by Williamson [11], although enlightening, might be subject to some blockage effects.

Adopting the non-dimensional parameters used by Williamson [11], the Reynolds number is defined on the basis of a single cylinder diameter with a spacing parameter g^* defined as

$$g^* = \frac{G}{D}. \tag{17}$$

Here G is the minimum distance between the cylinder surfaces and D is the cylinder diameter. When the cylinders are in very close proximity, $g^* < 1.0$, the flow is known to be in the asymmetric regime where the gap flow deflects to one side or the other, switching intermittently [11]. The resulting wake for this flow regime is found to be disordered and therefore of limited use for quantitative comparison. However when the spacing is increased beyond $g^* > 1.0$, the cylinders shed in a synchronised manner either in anti-phase or in-phase (with respect to the lift variation). These two modes are illustrated in Fig. 2. In experiment, the flow *flips* between these two modes but remains in either for large numbers of cycles. The vortex pattern is orderly particularly in the anti-phase mode which makes smoke visualisation photographs suitable for validation purposes.

3.2.1. Side-by-side arrangement

The flow interaction with two cylinders in a side-by-side arrangement has received extensive detailed experimental investigations by Williamson [11]. Thus, there exists well documented evidence with descriptions of the associated flow regimes and phenomena.

Experimentally it has been found that, at low Reynolds number, the wake switches between two modes of shedding as illustrated in Fig. 2. These are referred to as the in-phase and anti-phase shedding patterns with respect to the variation of the lift coefficient. A comprehensive study of these two shedding modes was carried out by Williamson [11]. It was found that each

Table 7
Values of Strouhal number, lift and drag coefficients for an isolated cylinder at $Re = 200$ determined by other methods

Investigator	Method	S	C_D (time average)	C_L (peak to peak)
Braza et al. [26]	Finite volume	0.2	1.32	1.55
Henderson [27]	Spectral ele.	–	1.341	–
Li et al. [5]	Finite ele.	0.18/0.187[a]	1.17/1.04[aa]	1.0/1.12[a]
Slaouti and Stansby [28]	Discrete vort.	0.196	–	1.25
Williamson and Brown[b] [29]	Spectral ele.	0.197	–	–
Zhang and Zhang [30]	Finite volume	0.197	–	–
Present work	Cell BEM	0.196	1.36	1.43

[a] Depending on outflow boundary conditions.
[b] Curve fit from data provided by R.D. Henderson.

mode remained stable for many cycles although the flow was capable of changing modes at any time due to perturbations arising during the experiment.

With the cell BEM it was found that for spacings of approximately $g^* > 1.5$ it was possible for either mode to be computed for large numbers of shedding cycles (greater than 20, say). The initial acceleration of the flow typically caused the cylinders to shed in anti-phase. However, imposing an oscillatory inflow of similar frequency to the shedding for a short duration caused the in-phase shedding to be established and to continue indefinitely even though the perturbation had ceased many shedding cycles before. This behaviour was consistent with observations recorded during the experiment. Changes in the strength and duration of the perturbation had no effect on the in-phase shedding frequency after transient effects had disappeared.

A comparison between an experimental flow visualisation and a numerical particle simulation was undertaken. To do this, two photographs were taken from Williamson [11] showing the wakes in the in-phase and anti-phase shedding modes at $Re = 100$ and $g^* = 3.0$. Although the exact location of the cylinders is not clear from the photographs, because they are obscured by smoke, it was possible to determine an approximate length scale based on their spacing. Once this was known the vortex spacings in the wake were also fixed. The vortex spacings were then used as a check for similarities between the vortex wakes of the computations and the experiment.

Fig. 11 shows the experiment with the computational wake for the anti-phase shedding, to the same scale. Given the uncertainty in determining the exact location of the cylinder centres, agreement of the location of the vortices in the wake, even at 37 diameters downstream, is very good.

Fig. 12 shows the experiment with the computational wake for the in-phase shedding, to the same scale. The idealised in-phase vortex configuration is unstable which can be seen in the distorted smoke filaments of the photograph. The computation also has an instability in the wake. The vortex pattern upstream of this instability is very similar to the experimental smoke visualisation. However, it seems there is slightly more asymmetry in the far wake of the computation as compared with the experiment.

Table 8 illustrates the calculated data corresponding to Williamson's experiment — no equivalent measured data are availible.

Table 8
The shedding frequency S, drag coefficient C_D and lift coefficient C_L for two cylinders side-by-side at ($g^* = 3.0$, $Re = 100$, the values for both shedding modes are shown)

Shedding mode	Cylinder	S	C_D	−ve	+ve	C_L	−ve	+ve
Anti-phase	1	0.173	1.45	−0.01	0.04	−0.08	−0.42	0.42
	2	0.173	1.45	−0.01	0.04	0.08	−0.42	0.42
In-phase	1	0.172	1.44	−0.01	0.05	−0.08	−0.32	0.32
	2	0.171	1.44	−0.01	0.05	0.08	−0.33	0.33

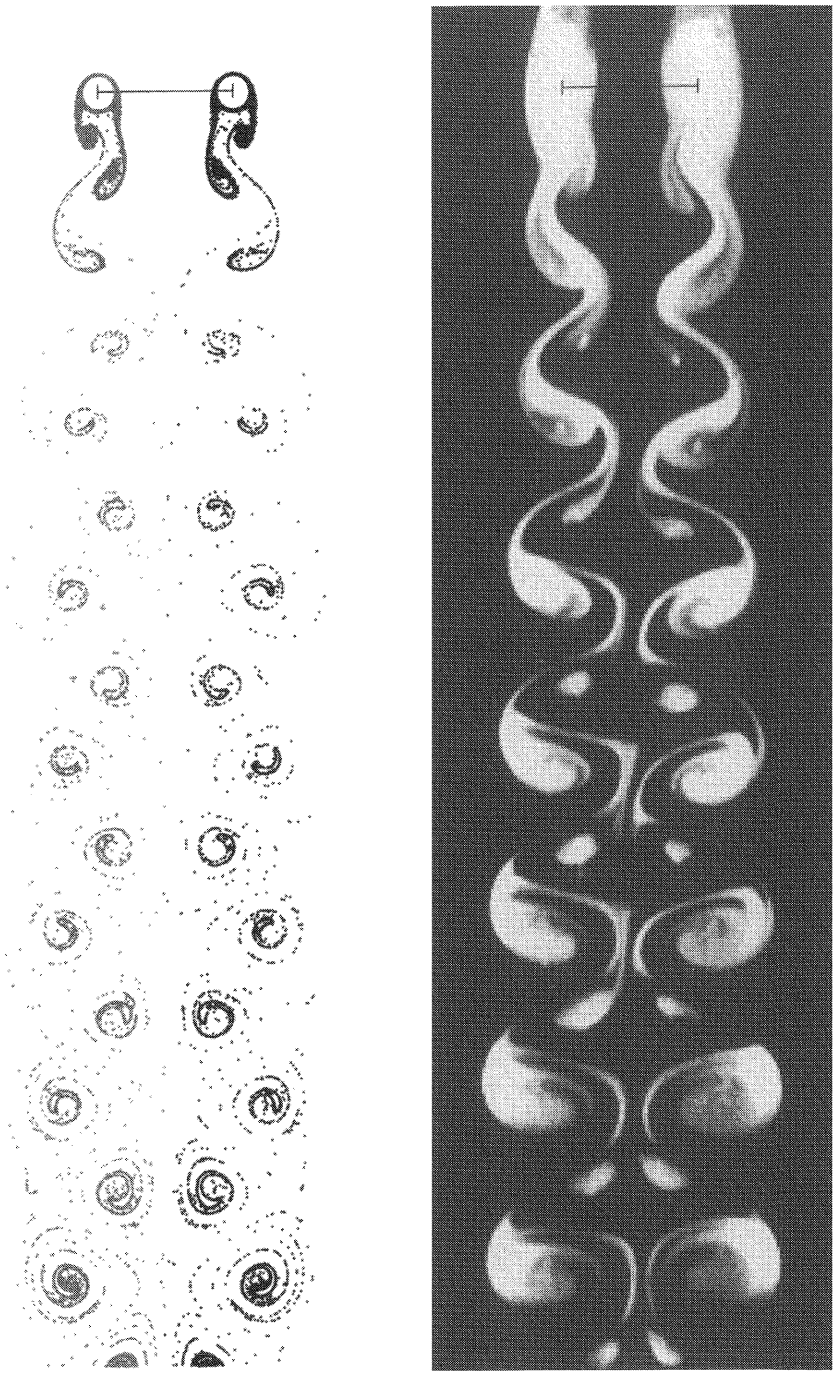

Fig. 11. A comparison of experiment and computation for two cylinders side-by-side at $Re = 100$ and $g^* = 3.0$ shedding in anti-phase. The photograph is taken from Williamson [11]. The superimposed bar scales are drawn between the assumed location of the cylinder centres.

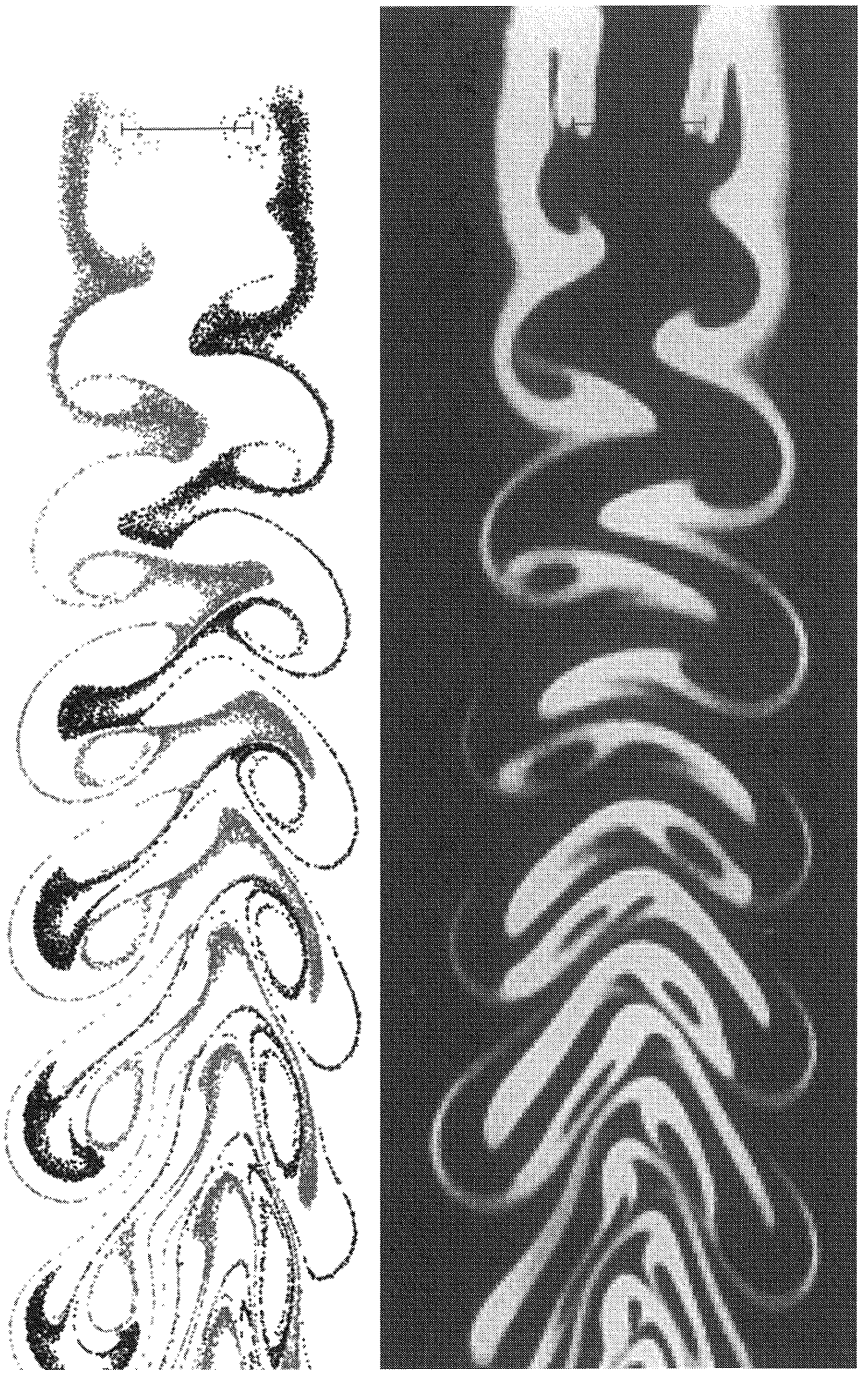

Fig. 12. A comparison of experiment and computation for two cylinders side-by-side at $Re = 100$ and $g^* = 3.0$ shedding in phase. The photograph is taken from Williamson [11]. The superimposed bar scales are drawn between the assumed location of the cylinder centres.

3.2.2. Tandem arrangement

For the tandem arrangement there is a shortage of quantitative and detailed experimental data which are appropriate for validation of flow solutions at low Reynolds numbers. However, it is reported by authors such as Zdravkovich [3] that when the cylinder spacing is $g^* > 3.8$ the upstream cylinder sheds in synchronisation with the downstream one. To demonstrate that the cell boundary element method is capable of predicting such flows without further modification, a computation was performed for the flow around two cylinders in tandem at $Re = 200$ and $g^* = 4.0$. The extents of the mesh boundaries and mesh refinement were chosen in the light of the study performed for the isolated circular cylinder at $Re = 200$ (see previous section). The shedding from both cylinders can be seen from the particle simulation shown in Fig. 13. The time averaged force coefficients and their deviations from the mean are shown for both cylinders in Table 9. The identical Strouhal frequencies confirm that the shedding is synchronised, in agreement with experiment.

4. Conclusions

Steady state and time dependent, vortex shedding flows, were computed using a second order time stepping numerical scheme within a cell boundary element method [8]. This mathematical model utilises an unstructured fluid domain idealisation and a primitive variable formulation. Although this paper focuses on two-dimensional fluid flows, the adoption of primitive variables allows a relatively simple extension of the model to describe three-dimensional flows.

The cell boundary element method applied to flows around an isolated cylinder or around two cylinder arrangements required no modifications to the mathematical model or numerical algorithms. The literature strongly suggests that this is in marked contrast with other mathematical models (i.e. a vorticity–stream function formulation) applied to single or connected fluid domains.

Comparisons with experimental evidence, other presented computations and the findings from the cell boundary element method for flows around an isolated circular cylinder and two cylinder arrangements (focusing on the side-by-side arrangement) are presented, discussed and in general, a very satisfactory level of agreement demonstrated.

Fig. 13. A particle simulation of the flow field around two cylinders in tandem at $Re = 200$ (based on one cylinder diameter) and $g^* = 4.0$. The distance between the cylinder centres is 5 diameters and the length of wake is 14 diameters behind the last cylinder.

Table 9
The shedding frequency S, drag coefficient C_D and lift coefficient C_L for the cylinders in tandem at $g^* = 4.0$, $Re = 200$

Cylinder	S	C_D	−ve	+ve	C_L	−ve	+ve
1	0.179	1.25	−0.05	0.07	0.00	−0.71	0.71
2	0.179	0.38	−0.18	0.23	−0.00	−1.59	1.59

For the isolated cylinder, agreement was very good between experimental measurements and predictions of vortex shedding frequencies and forces affecting the bluff body. Sensitivity studies of the influence of boundary conditions and locations on flow characteristics, when modelling an infinite domain, showed that the proposed method was robust in this respect.

For computations involving side-by-side cylinder arrangements, vortex shedding occurred naturally either in the anti-phase or in-phase modes as displayed in Fig. 2. A small perturbed inlet flow could be applied to encourage computation in one mode or the other. Each mode continued for large numbers of cycles (>20), unless perturbed by changing the boundary conditions.

Particle streak line simulations, generated from the cell boundary element method velocity fields [8], provide the principal means of comparison with the smoke visualisation photographs of the experiments performed by Williamson [11]. Striking similarities of the detailed wake structures are observed between the predicted particle simulation and the photographs of experiments as demonstrated in Figs. 11 and 12.

References

[1] Sarpkaya T, Isaacson M. Mechanics of wave forces on offshore structures. New York: Van Nostrand Reinhold, 1981.
[2] Williamson CHK. Vortex dynamics in the cylinder wake. Ann Rev Fluid Mech 1996;28:477–539.
[3] Zdravkovich MM. Review of flow interference between two circular cylinders in various arrangements. J Fluids Engrg, Trans ASME 1977;99(4):618–33.
[4] Chang K, Song C. Interactive vortex shedding from a pair of circular cylinders in a transverse arrangement. Int J Numer Methods Fluids 1990;11:317–29.
[5] Li J, Chambarel A, Donneaud M, Martin R. Numerical study of laminar flow past one and two cylinders. Comput & Fluids 1991;19(2):155–70.
[6] Johnson AA, Tezduyar TE, Liou J. Numerical simulation of flows past periodic arrays of cylinders. Comput Mech 1993;11:371–83.
[7] Mittal S, Kumar V, Raghuvanshi A. Unsteady incompressible flows past two cylinders in tandem and staggered arrangements. Int J Numer Methods Fluids 1997;25:1315–44.
[8] Tan M, Farrant T, Price WG. A cell boundary element method for viscous laminar flow solutions. Proc Roy Soc Lond A 1999;455:4277–304.
[9] Price WG, Tan M. Applications of viscous boundary element method in hydrodynamic problems relating to manoeuvering bodies. In: Proc. 19th Symp. on Naval Hydrodynamics. Seoul, Korea: Office of Naval Research, 1992. p. 437–47.
[10] Farrant T. The boundary element method applied to viscous and vortex shedding flows around cylinders.

Ph.D. thesis, Department of Ship Science, Faculty of Engineering and Applied Science, University of Southampton, May 1999.
[11] Williamson CHK. Evolution of a single wake behind a pair of bluff bodies. J Fluid Mech 1985;159:1–18.
[12] Tan M. A viscous boundary element approach to fluid flow-structure interaction problems. Ph.D. thesis, Department of Ship Science, Faculty of Engineering and Applied Science, University of Southampton, April 1994.
[13] Tosaka N, Kakuda K. The generalised boundary element method for nonlinear problems. In: Brebbia CA, editor. Boundary Elements X. Proceedings of the 10th International Conference Boundary Element Methods, Southampton. Computational Mechanics Publications, 1988.
[14] Price WG, Tan M. The calculation of fluid actions on manoeuvring arbitrary shaped submerged bodies using viscous boundary elements. In: Proc. 18th Symp. Naval Hydrodynamics. Ann Arbor, MI, USA: Office of Naval Research, 1990. p. 804–14.
[15] Brebbia CA. The boundary element method for engineers. London: Pentech Press, 1978.
[16] Brebbia CA, Walker S. Boundary element techniques in engineering. Newness-Butterworths, 1980.
[17] Brebbia CA, Walker S. Steady and unsteady potential problems using the boundary element method. In: Recent advances in numerical methods in fluids, vol. 1. Swansea, UK: University College Swansea, Pinridge Press, 1980. p. 1–15.
[18] Press WH, Flannery BP, Teukolsky SA, Vetterling WT. Numerical recipes in C, the art of scientific computing. Cambridge: Cambridge University Press, 1993.
[19] Cook RD, Malkus DS, Plesha ME. Concepts and applications of finite element analysis. New York: Wiley, 1989.
[20] Bathe K-J, Wilson EL. Numerical methods in finite element analysis. Englewood Cliffs, NJ, USA: Prentice-Hall, 1976.
[21] Fornberg B. Steady viscous flow past a circular cylinder up to Reynolds number 600. J Comput Phy 1985;61:297–320.
[22] Farrant T, Tan M, Price WG. A cell boundary element method applied to laminar vortex shedding from arrays of cylinders in various arrangements. J Fluids & Struct 2000;14(3):375–402.
[23] Behr M, Hastreiter D, Mittal S, Tezduyar TE. Incompressible flow past a circular cylinder: dependence of the computed flow field on the location of the lateral boundaries. Comput Methods Appl Mech Engrg 1995;123:309–16.
[24] Tezduyar TE, Shih R. Numerical experiments on downstream boundary of flow past a cylinder. J Engrg Mech 1991;117:854–71.
[25] Williamson CHK. 2D and 3D aspects of the wake of a cylinder, and their relation to wake computations. Lect Applied Math 1991;28:719–51.
[26] Braza M, Chassaing P, Minh HH. Numerical study and physical analysis of the pressure and velocity fields in the near wake of a circular cylinder. J Fluid Mech 1986;165:79–130.
[27] Henderson RD. Details of the drag curve near the onset of vortex shedding. Phys Fluids 1995;7(9):2102–4.
[28] Slaouti A, Stansby PK. Flow around two circular cylinders by the random vortex method. J Fluids & Struct 1992;6:641–70.
[29] Williamson CHK, Brown GL. A series in $(1\sqrt{Re})$ to represent the Strouhal–Reynolds number relationship of the cylinder wake. J Fluids & Struct 1998;12(8):1073–85.
[30] Zhang H, Zhang X. Flow structure analysis around an oscillating circular cylinder at low KC number: a numerical study. Comput & Fluids 1997;26(1):83–106.